




RESEARCH ARTICLE | JANUARY 31 2024

# Solute-enhanced twin boundary migration in CuAg alloy

Dengke Chen ; Yin Zhang ; Shuozhi Xu  



*J. Appl. Phys.* 135, 045104 (2024)

<https://doi.org/10.1063/5.0176708>



CrossMark



**APL Machine Learning**  
**Latest Articles Online!**  
**Read Now**



# Solute-enhanced twin boundary migration in CuAg alloy

Cite as: J. Appl. Phys. 135, 045104 (2024); doi: 10.1063/5.0176708

Submitted: 15 September 2023 · Accepted: 8 January 2024 ·

Published Online: 31 January 2024



Dengke Chen,<sup>1</sup> Yin Zhang,<sup>2</sup> and Shuozi Xu<sup>3,a)</sup>

## AFFILIATIONS

<sup>1</sup>Department of Engineering Mechanics, School of Naval Architecture, Ocean and Civil Engineering, Shanghai Jiao Tong University, Shanghai 200240, China

<sup>2</sup>Department of Mechanics and Engineering Science, College of Engineering, Peking University, Beijing 100871, China

<sup>3</sup>School of Aerospace and Mechanical Engineering, University of Oklahoma, Norman, Oklahoma 73019, USA

<sup>a)</sup>Author to whom correspondence should be addressed: shuozhixu@ou.edu

## ABSTRACT

Understanding the mechanical behavior of nanotwinned materials in alloys is essential, particularly in relation to solute-influenced twin boundary (TB) migration. This research employs atomistic simulations and theoretical analysis to explore the influence of solute atoms on TB migration in CuAg alloys. Contrary to conventional beliefs, simulations reveal that solute Ag atoms enhance TB migration, challenging established perceptions. Nudged elastic band calculations confirm that Ag solutes substantially reduce energy barriers, shedding light on the mechanism driving solute-enhanced TB migration. This work opens novel avenues for investigating point defect impacts on TB mobility, offering insights into alloy element roles in grain boundary migration and polycrystalline material properties.

Published under an exclusive license by AIP Publishing. <https://doi.org/10.1063/5.0176708>

## I. INTRODUCTION

Nanotwinned metals have garnered significant attention in recent years due to their remarkable strength and ductility properties.<sup>1–5</sup> Nanotwinned face-centered-cubic (FCC) metals are engineered by introducing twin boundaries (TBs) within ultra-fine crystalline metals, resulting in a grain size of a few hundred nanometers.<sup>6–8</sup> Studies have revealed that these TBs effectively hinder dislocation motion, leading to the Hall–Petch-type strengthening mechanism. Moreover, TBs serve as slip planes for FCC metals, enabling them to accommodate large plastic strains.<sup>9–11</sup> Consequently, gaining a quantitative understanding of TB-mediated processes, such as migration, sliding, and defect interactions, becomes critical for optimizing the properties of nanotwinned structures.

TBs are known to be shear-coupled grain boundaries (GBs).<sup>12–14</sup> Typically, shear-coupled GBs move in the direction normal to the GB plane due to the shear stress parallel to the GB plane.<sup>15</sup> There is an intrinsic geometric factor known as the coupling factor,  $\beta = V/V_M$ , characterizing the ratio between the applied parallel velocity  $V$  and the normal migration velocity  $V_M$ . Based on this, a series of studies have investigated the influence of

impurities on GB motion in both pure metals and alloys. The conventional opinion is that point defects inhibit the GB motion. Numerous corresponding experimental and simulated evidence can be found in previous literatures.<sup>16–21</sup> However, recent studies have reported that vacancies might enhance GB sliding<sup>22</sup> and migration<sup>23</sup> in FCC metals and even facilitate TB migration in body-centered-cubic (BCC) metals.<sup>24</sup> Many researchers have believed that GB migration is accomplished through the nucleation and propagation of disconnections at GBs.<sup>25–27</sup> Consequently, the abnormal phenomena mentioned above can be attributed to the opinion that certain point defects could reduce the disconnection nuclear barrier, thus enhancing GB sliding or migration.<sup>23</sup> These studies underscore the significance of the role of point defects in disconnection nucleation during the GB motion process and inspire us to explore the impact of point defects on TB migration in FCC metals.

To gain insight into the elementary process of TB migration, researchers have employed *in situ* transmission electron microscopy (TEM) experiments and molecular dynamics (MD) simulations to explore TB migration in nanocrystalline copper (Cu). Wang *et al.* provided the experimental evidence in pure Cu that TB migration occurs via twinning dislocation emission from the TB/GB

31 January 2024 14:02:53

intersections, facilitating the twinning dislocation nucleation.<sup>28</sup> Zhang *et al.* performed MD simulations to explore the TB migration both without and with defects, including steps and interstitial atoms, and found that the critical shear stress (CSS) required for defective TB migration was lower than that for perfect TB.<sup>29</sup> Both studies suggest that the defects might enhance TB migration. In the case of alloys, particularly the medium/high entropy alloys, TB-mediated deformation is one of the most important mechanisms. Atomistic simulations suggest that the medium/high entropy alloys have low stacking fault energies and a high propensity for twinning, in which the stable twin architectures serve as a continuous source of strength, ductility, and toughness.<sup>30–33</sup> Therefore, it becomes essential to investigate the role of the solute atoms in TB migration and determine whether these atoms impede or enhance TB migration.

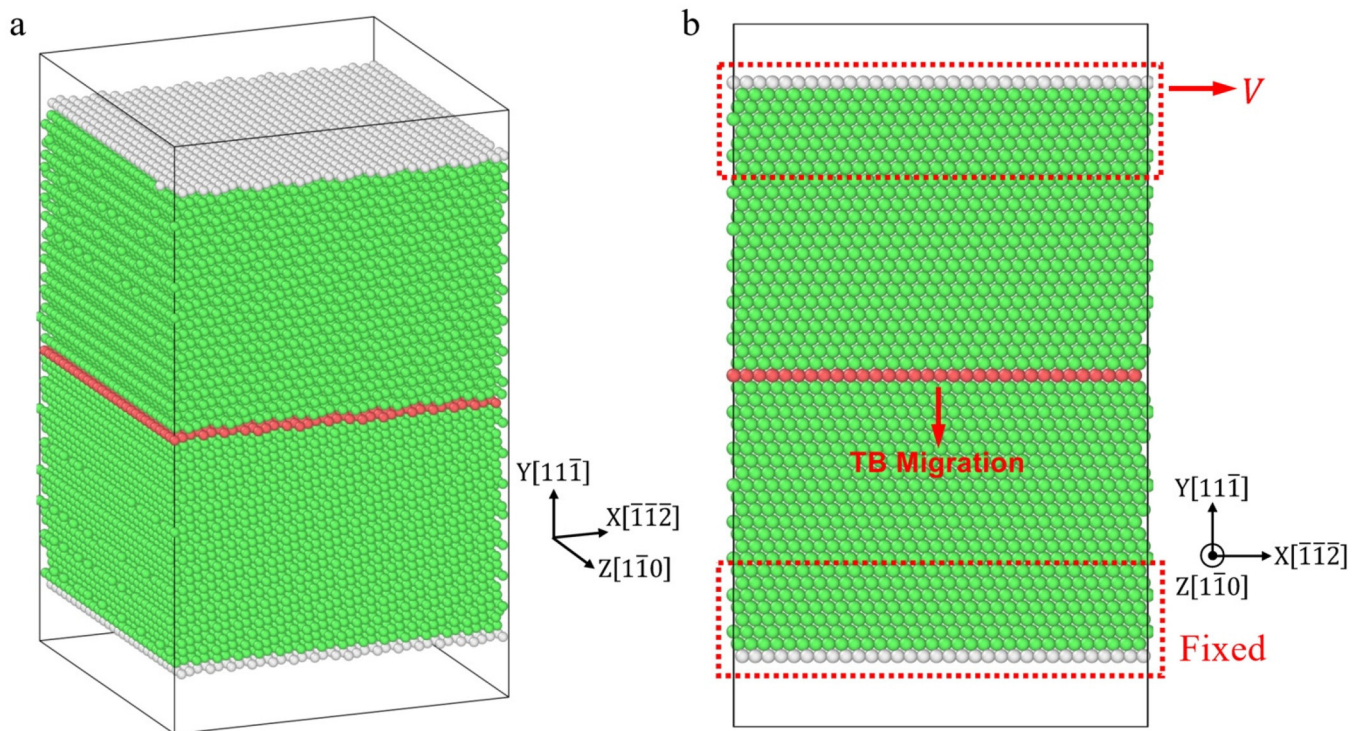
In this study, we investigate how solute atoms influence TB migration in CuAg alloys using atomistic simulations and theoretical analysis. Our simulations unveil that solute Ag atoms play a role in decreasing the CSS of TB migration in CuAg alloys, thereby facilitating the process. This discovery challenges conventional wisdom, as solute atoms are often traditionally regarded as GB migration inhibitors. Through nudged elastic band (NEB) calculations, we firmly establish that solute Ag atoms effectively reduce the energy barrier of TB migration, clarifying the phenomenon of

solute-enhanced TB migration. The rest of the paper is organized as follows. Section II presents MD simulations of shear-coupled TB migration, investigating the influence of temperature and solute content on TB migration. In Sec. III, we conduct NEB calculations to reveal the solute-induced reduction in the activation energy of TB migration. Section IV discusses the underlying mechanism of this abnormal observation. Finally, Sec. V provides concluding remarks to summarize our findings.

## II. ATOMISTIC MODELING OF TB MIGRATION

### A. MD simulation setup

To explore the effect of the temperatures and solute atoms on TB migration, we performed MD simulations to study the shear-coupled TB migration process in pure Cu and Cu–Ag systems, respectively. Figure 1 presents the detailed atomic configurations of the simulation setup for pure Cu. The simulation cell has the dimension of  $7 \times 10 \times 7 \text{ nm}^3$  and contains a total of  $\sim 43\,000$  Cu atoms. Periodic boundary conditions are imposed in both the  $X - [\bar{1}\bar{1}\bar{2}]$  and  $Z - [\bar{1}\bar{1}0]$  directions, while the top and bottom surfaces are traction free along the  $Y - [11\bar{1}]$  direction. For the Cu–Ag system, Cu atoms are randomly substituted with varying fractions of Ag atoms.



31 January 2024 14:02:53

**FIG. 1.** MD simulation setup of TB migration in the (a) perspective view and (b) side view. The shear stress is applied by moving the top slab (denoted by red-dotted square) with a constant velocity  $V$  in the  $X - [\bar{1}\bar{1}\bar{2}]$  direction. Here, the atomic structure visualization tool OVITO (Ref. 34) is used for a common neighbor analysis, so as to identify the atoms at the surface (gray), the atoms with FCC structure (green), and atoms in the twin boundary (red).

Simulations are performed using LAMMPS<sup>35</sup> at various temperatures. The visualization tool OVITO is used to perform the common neighbor analysis to clearly display the TB structure. Two 1.5-nm-thick slabs are fixed at the top and bottom surfaces of the simulation cell. At 0 K, the shear load is exerted by imposing a displacement-controlled boundary condition on the top slab in the  $X - [\bar{1}\bar{1}\bar{2}]$  direction, while the bottom slab is held fixed, and then the energy minimization process is performed through the conjugate gradient method. At finite temperatures, the top slab is imposed a constant velocity  $V = 0.01 \text{ \AA/ps}$  in the  $X - [\bar{1}\bar{1}\bar{2}]$  direction to maintain a constant shear strain rate of  $\dot{\gamma} \approx 10^8 \text{ s}^{-1}$  in the canonical ensemble.<sup>15</sup>

The embedded atom method (EAM) potential by Mishin *et al.*<sup>36</sup> is employed. This EAM potential has been widely used in many atomistic modeling works.<sup>19,37,38</sup> Since TB migration is intricately linked with the nucleation of TB dislocation,<sup>39</sup> understanding the influence of solute atoms on homogeneous dislocation nucleation becomes pivotal when modeling TB migration. Consequently, the utilization of a reliable EAM potential is critical, ensuring an accurate representation of stacking fault energy curves associated with the difficulty of homogeneous dislocation nucleation. In Fig. 2, we present the stacking fault energy curves for pure Cu and CuAg alloys, obtained through molecular statics (MS) calculations<sup>40</sup> with the current EAM potential and the density functional theory (DFT) calculations using VASP.<sup>41</sup> Notably, both MS and DFT calculations exhibit consistent trends, revealing that the introduction of solute atoms leads to a reduction in unstable stacking fault energy. Therefore, this observed alignment between the two

methods establishes the reliability of this EAM potential for modeling TB migration.

## B. Representative results of TB migration

TB is a shear-coupled grain boundary,<sup>12</sup> i.e., applied shear stress would cause the TB migration in the direction perpendicular to the TB plane, as denoted in Fig. 1(b). Figure 3 depicts the representative simulation results of TB migration at 500 K, where the TB exhibits the stick-slip motion. The shear stress increases with increasing strain, causing the TB to slip in the shear direction. When the shear stress reaches a critical value, denoted as  $\tau_c(T = 500 \text{ K})$ , the TB undergoes a sudden jump to a new equilibrium position (i.e., in the negative Y direction), marked by a step of height  $H$ . The bicrystal experiences a permanent shear deformation and a subsequent stress drop.

As the shear strain continues to increase, the stress gradually builds up again until it reaches the CSS level  $\tau_c(T = 500 \text{ K})$ , at which point the TB undergoes another jump. This repetitive process leads to the incremental forward motion of the TB by a distance  $H$ . Throughout this motion, the shear stress exhibits a characteristic saw-tooth behavior, as depicted by a brown-square curve in Fig. 3. The stepwise movement of TB, as denoted by a black-dotted curve in Fig. 3, can be extracted by the characteristic parameters through curve fitting, i.e., migration velocity  $V_M = 1.53 \text{ m/s}$ . Then, the simulated coupling factor  $\beta = V/V_M = 0.65$ , which is close to the theoretical value of 0.71 in the literature.<sup>42</sup>

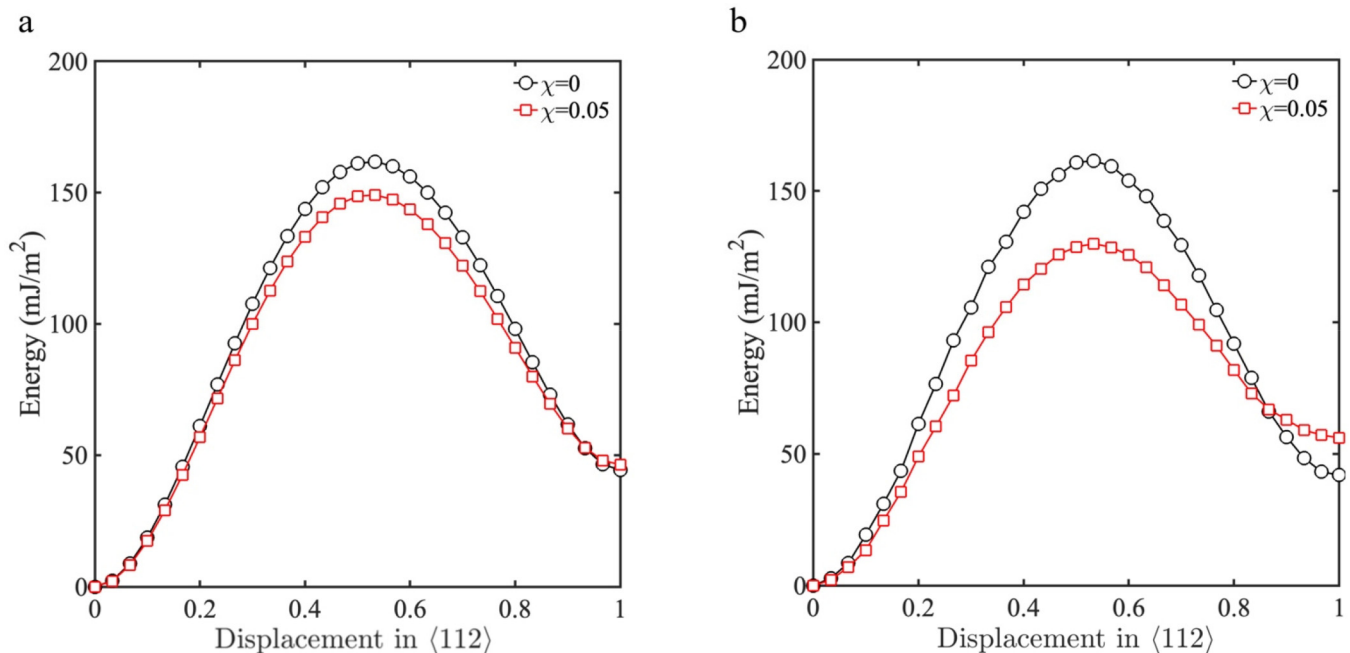


**FIG. 2.** General stacking fault energy curves for pure Cu (black circles) and CuAg alloy (red squares). (a) MS calculations based on the current EAM potential. (b) DFT calculation results using VASP software.



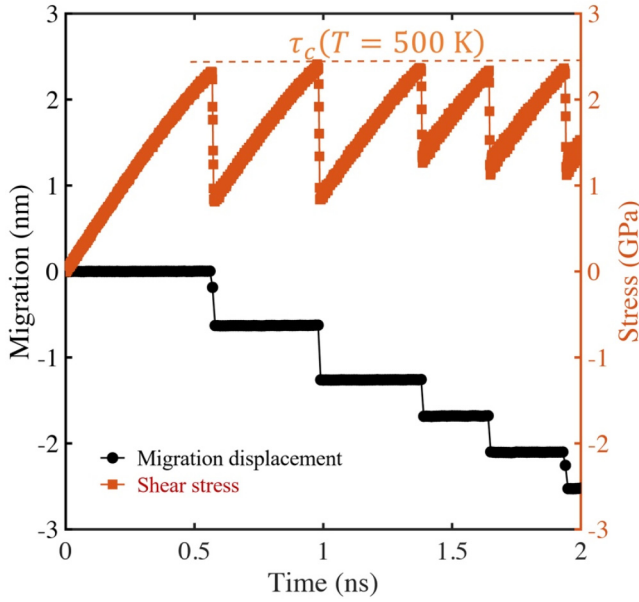


**FIG. 3.** MD simulation results of shear-coupled TB migration at 500 K. TB moves in the stick-slip pattern, as shown in black dots. The stress exhibits a saw-tooth behavior with a peak value  $\tau_c(T = 500 \text{ K})$ , as shown in brown squares.

### C. Temperature effect in pure Cu

To reveal the effect of temperature on the CSS of TB migration, we performed a series of MD simulations for various temperatures, ranging from 0 to 500 K. Figure 4 shows the normalized CSS for TB migration as a function of normalized temperatures. Curve fitting reveals that there exists a linear relationship. To be specific,

$$\frac{\tau_c(T)}{\tau_{c0}} = 1 - A \frac{T}{T_m}. \quad (1)$$

Here,  $\tau_c(T)$  is the CSS at finite temperature  $T$ ;  $\tau_{c0}$  is the CSS at 0 K;  $A = 0.72$  is a dimensionless material constant, depending on the strain rate and other factors (see Sec. III A). It is noted that in previous literature,<sup>43,44</sup> the CSS of general GB has consistently been described using the exponential form with respect to temperature  $T$ , i.e.,

$$\frac{\tau_c(T)}{\tau_{c0}} = 1 - B \left( \frac{T}{T_m} \right)^{2/3}. \quad (2)$$

Hence, the special temperature-dependent relation of TB migration in Eq. (1) may be attributed to the special stress-dependent activation energy, which will be explained in Sec. III B.

### D. Solute effect in CuAg

To investigate the solute effect on TB migration, we conducted a series of MD simulations in which we randomly

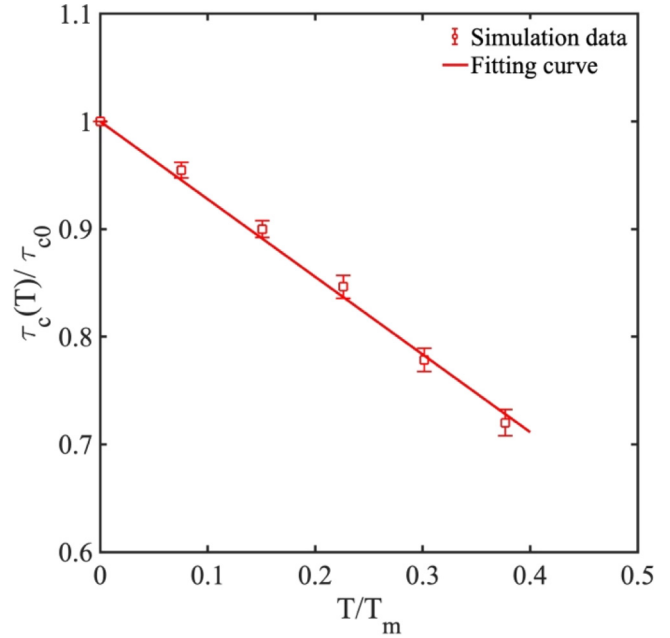


**FIG. 4.** Normalized critical shear stress (CSS)  $\tau_c(T)/\tau_{c0}$  as functions of the normalized temperature  $T/T_m$  in Cu. Here,  $\tau_c(T)$  represents the CSS at various temperatures  $T$ , while  $\tau_{c0} = 2.98 \text{ GPa}$  signifies the CSS at 0 K. The melting temperature  $T_m$  is 1327 K. The mean values are obtained by averaging the results from 10 samples with different random atom velocities. The error bars in the figure correspond to the standard deviation.

substituted Cu atoms with Ag atoms at various temperatures, ranging from 0 to 500 K. In Fig. 5, we present the results, showing the normalized critical stress  $\tau_{c0}^\chi/\tau_{c0}$  for TB migration as a function of solute fraction  $\chi$  at 0 K. The data points denoted by red-solid circles indicate that as the Ag fraction  $\chi$  increases, the normalized CSS  $\tau_{c0}^\chi/\tau_{c0}$  decreases. Curve fitting reveals that the fraction-dependent relationship follows a linear trend described by the following equation:

$$\frac{\tau_{c0}^\chi}{\tau_{c0}} = 1 - D\chi. \quad (3)$$

Here, the dimensionless material constant  $D$  is obtained from the curve fitting and depends on a series of material properties. These findings clearly demonstrate that the presence of solute Ag atoms reduces the CSS in CuAg alloys, thereby facilitating the TB migration.

To explore the effect of shear modulus on the reduction of CSS, we calculated the fraction-dependent shear modulus in CuAg alloys, as depicted in Fig. 5(b). The results indicate an increase in shear modulus with increasing solute Ag atoms, which confirms that the reduced critical stress is not caused by the shear modulus. After excluding the effect of shear modulus, we extracted the new normalized critical stress  $(\tau_{c0}^\chi/\mu^\chi)/(\tau_{c0}/\mu^0)$ , represented by blue-square data points in Fig. 5(a). Notably, the new normalized CSS

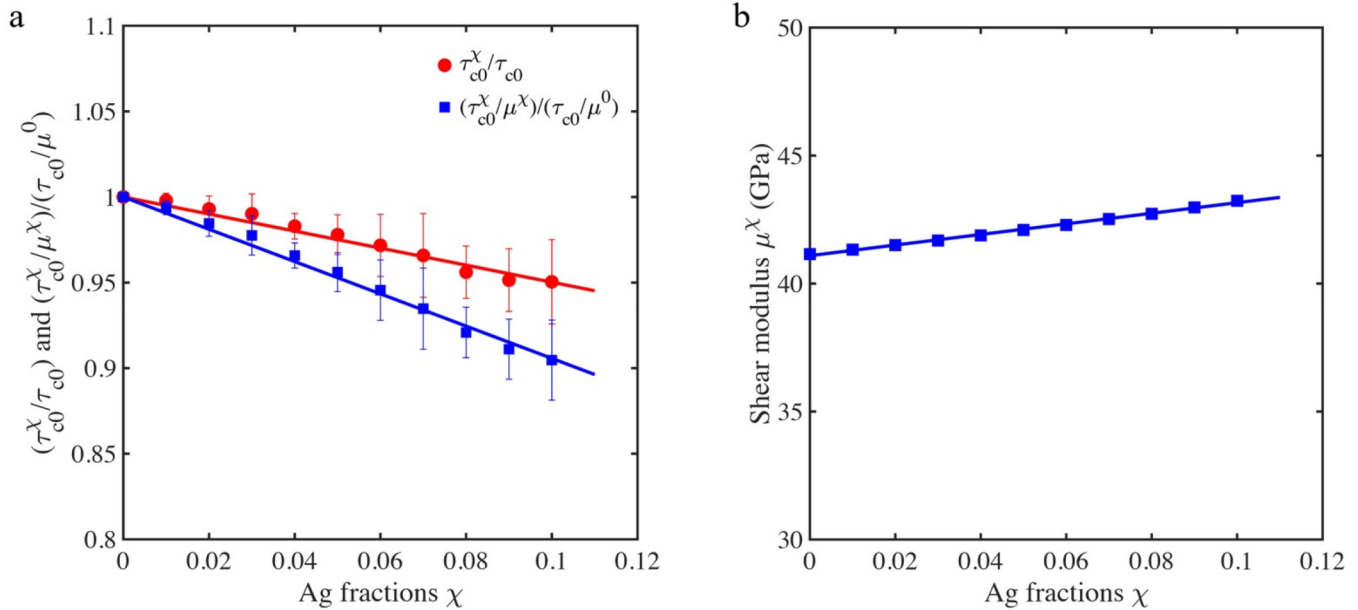


**FIG. 5.** Fraction-dependent CSS and shear modulus at 0 K. (a) Normalized CSS  $\tau_{c0}^{\chi}/\tau_{c0}$  and  $(\tau_{c0}^{\chi}/\mu^{\chi})/(\tau_{c0}/\mu^0)$  as functions of solute Ag fractions  $\chi$  at 0 K. Here,  $\tau_{c0}^{\chi}$  is the CSS for the Ag fraction  $\chi$  at 0 K, and  $\mu^0$  is the shear modulus for pure Cu.  $\tau_{c0}$  has been defined as the CSS for pure Cu at 0 K. The mean values are obtained by averaging the results from 10 samples with different random atom velocities. The error bars in the figure correspond to the standard deviation. (b) Shear modulus  $\mu^{\chi}$  for CuAg alloy with Ag fractions  $\chi$ .

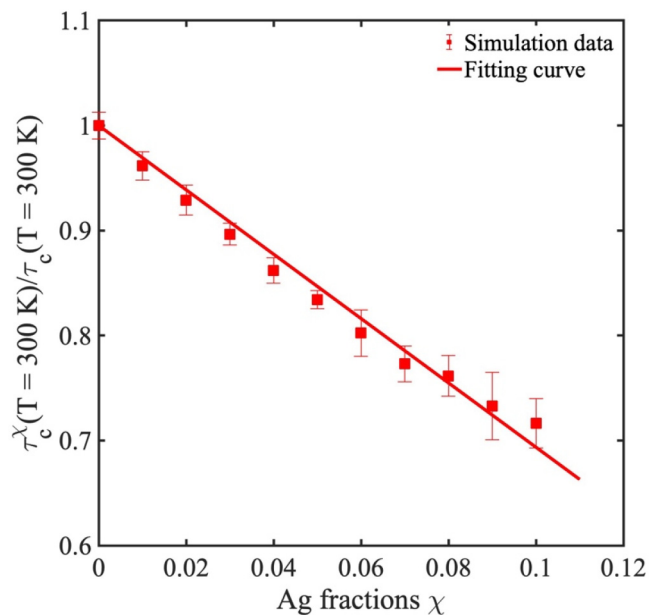
still decreases with increasing solute atoms. Curve fitting reveals the following relationship:

$$\frac{\tau_{c0}^{\chi}/\mu^{\chi}}{\tau_{c0}/\mu^0} = 1 - E\chi. \quad (4)$$

Here, the dimensionless material constant  $E = 0.94$  is larger than  $D = 0.50$  in Eq. (3), further confirming that the solute-reduced critical stress has an intrinsic mechanism independent of the shear modulus. This verification of the relation encourages the view that the ratio of the critical stress, measured in this way, is largely independent of the shear modulus and, thus, provides information about the nature of the elementary migration of TB.

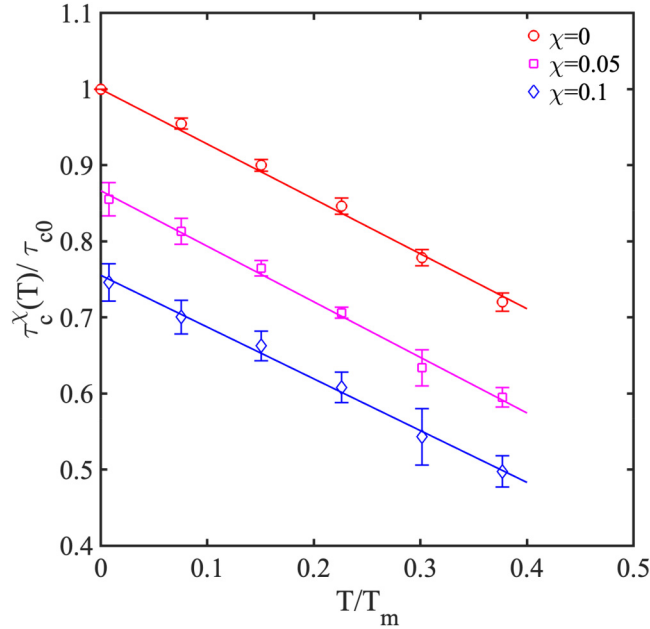
Figure 6 demonstrates the normalized critical shear stress vs solute fractions at 300 K, revealing that the solute-reduced critical stress is also present at finite temperatures. This abnormal observation of solute-reduced critical stress challenges our intuition and conventional knowledge. Previous literatures often report that solute atoms pin and prohibit GB migration.<sup>16–21</sup> However, in our previous paper,<sup>23</sup> we discovered that dilute vacancies enhance GB migration in Cu, and here, we present another compelling example of solute-enhanced TB migration.

Figure 7 presents the normalized critical shear stress (CSS)  $\tau_c^{\chi}(T)/\tau_{c0}$  as a function of the normalized temperature  $T/T_m$  in pure Cu ( $\chi = 0$ ) and CuAg alloys ( $\chi = 0.05, 0.1$ ). The solute-reduced critical shear stress of TB migration can be seen in any temperature. The curve fitting reveals that the linear



**FIG. 6.** Fraction-dependent normalized CSS in CuAg alloy at 300 K. Here,  $\tau_c^{\chi}(T = 300 \text{ K})$  is the CSS for CuAg alloy with Ag fraction  $\chi$  at 300 K.  $\tau_c(T = 300 \text{ K})$  is the CSS for pure Cu at 300 K. The mean values are obtained by averaging the results from 10 samples with different random atom velocities. The error bars in the figure correspond to the standard deviation.

31 January 2024 14:02:53



**FIG. 7.** Normalized CSS  $\tau_c^X(T)/\tau_{c0}$  as functions of the normalized temperature  $T/T_m$  in pure Cu and CuAg alloys. The mean values are obtained by averaging the results from 10 samples with different random atom velocities. The error bars in the figure correspond to the standard deviation.

dependence of normalized CSS on normalized temperatures exists under various solute fractions.

### III. NEB CALCULATION OF TB MIGRATION

#### A. Activation energy of TB migration

To investigate the underlying mechanism of solute-reduced CSS of TB migration, we performed atomistic simulations using the NEB method. A series of NEB calculations allow us to determine the minimum energy paths (MEPs) and associated activation energies (i.e., energy barriers) for TB migration in pure Cu and CuAg alloys. During the NEB calculations, 96 replicas/configurations are used to describe the MEP. For each time step, all replicas, including the first and end ones, are considered, with the first and end replicas fixed throughout the NEB calculation. The first replica represents the original TB configuration, while the end replica is a configuration in which the entire TB has migrated by a step with the same shear strain to the first replica. We prepare all intermediate candidate configurations by means of linear interpolation between the first and end replicas. After several time steps, they converge to the final configurations/replicas. More details can be referred to our previous paper.<sup>23</sup>

Figure 8(a) shows the converged MEP of TB migration under the shear stress  $\tau = 2.5$  GPa. Atomistic configurations along the MEP and their corresponding energies are plotted as red circles. In all the presented MEPs, the reaction coordinate is defined as the

normalized path length along the MEP, and the energy of the first replica on the MEP is taken to be zero. The atomistic configuration in Fig. 8(b) is the first state, corresponding to a local energy minimum on the MEPs. Figure 8(c) presents the atomistic configuration at the saddle-point state with energy barrier  $E_{Cu} = 0.99$  eV, in which the shape of the disconnection loop (with Burgers vector  $b = \frac{1}{6}[\bar{1}\bar{1}2]$ ) is close to an elliptic shape. Figure 8(d) shows the disconnection loop that propagates in the TB plane. As evident from Fig. 8, the TB moves in the negative Y direction via the nucleation and glide of twinning partial dislocation loops.

Similar NEB calculations are performed for CuAg alloy at the same shear stress to investigate the solute effect on TB migration, as shown in Fig. 9. It is evident that the solute Ag atoms reduce the activation energy from  $E_{Cu} = 0.99$  eV [Fig. 8(a)] to  $E_{CuAg} = 0.44$  eV [Fig. 9(a)]. Figure 9(c) reveals that the twinning dislocation nucleates around the solute Ag atoms (denoted by black atoms) and then propagates. As a result, the solute Ag atoms lower the activation energy of twinning dislocation nucleation and then facilitate the TB migration in CuAg alloys.

#### B. Stress-dependent activation energies

A series of NEB calculations are performed to verify the solute effect on TB migration. In Fig. 10, we show with red circles and blue squares for the calculated activation energies of TB migration in Cu and CuAg alloys, respectively, under various stresses. It is seen that the solute Ag atoms reduce the activation energy under the same shear stress. The reduction in migration barriers between pure Cu and CuAg alloy is not sensitive to the shear stress. Furthermore, curve fitting for TB migration in pure Cu shows that

$$E_{Cu}(\tau) = E_{Cu}^0 \left( 1 - \frac{\tau}{\tau_{c0}} \right). \quad (5)$$

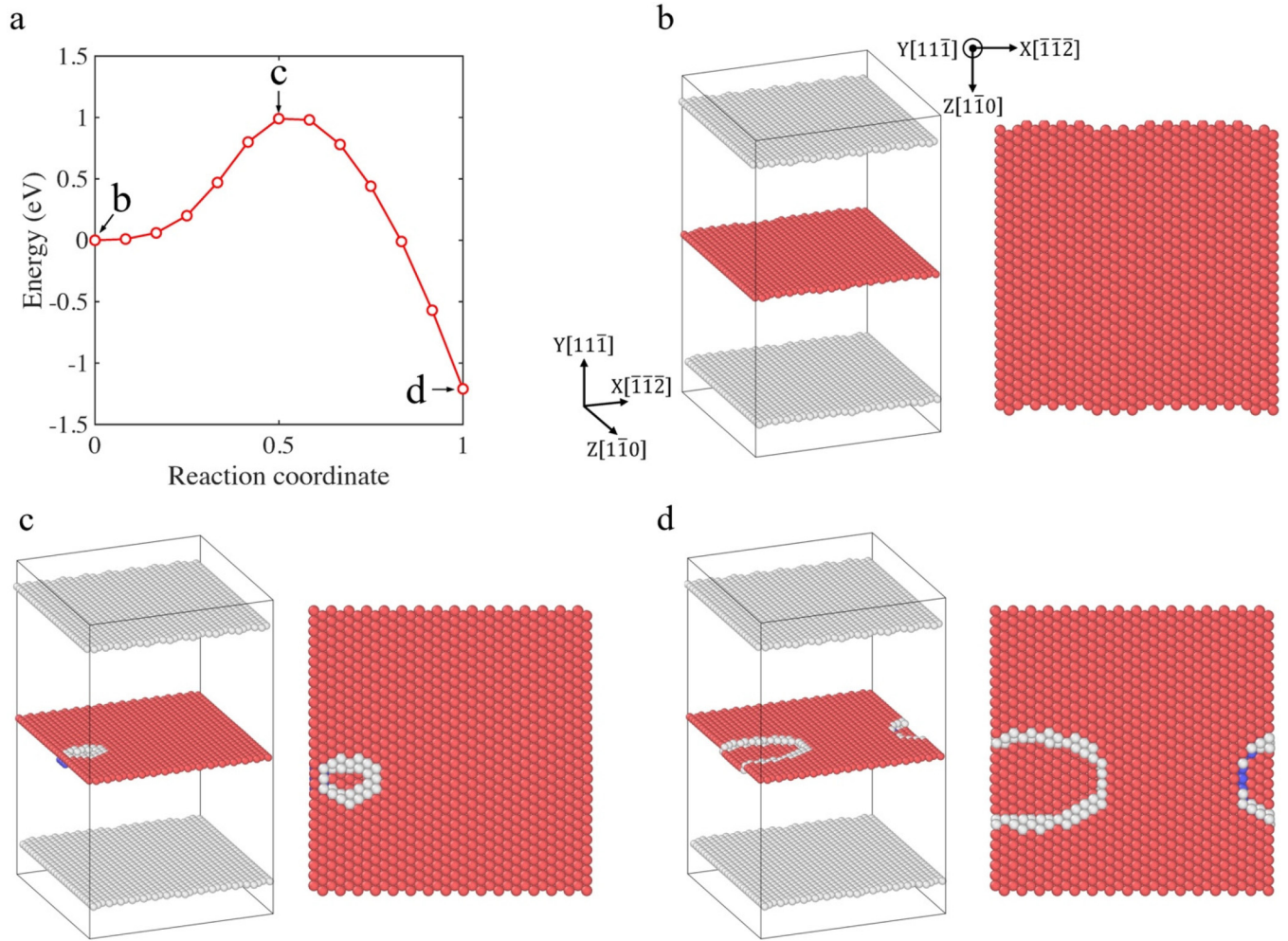
Here,  $E_{Cu}(\tau)$  is the activation energy of TB migration in pure Cu under the shear stress  $\tau$ .  $E_{Cu}^0 = 7.08$  eV is the activation corresponding to  $\tau = 0$ .  $\tau_{c0} = 2.98$  GPa has been defined as the critical stress for TB migration in pure Cu at 0K. In CuAg alloy, the stress-dependent activation energies also satisfy the linear relationship, i.e.,

$$E_{CuAg}(\chi, \tau) = E_{CuAg}^0(\chi) \left( 1 - \frac{\tau}{\tau_{c0}^X} \right). \quad (6)$$

Here,  $E_{CuAg}(\chi, \tau)$  is the activation energy of TB migration in CuAg alloy under the shear stress  $\tau$  for Ag fraction  $\chi$ . Curve fitting shows that the corresponding material properties for CuAg alloys with  $\chi = 0.05$  are  $E_{CuAg}^0(0.05) = 5.83$  eV and  $\tau_{c0}^X = 2.76$  GPa.

In the following, we will show that linearly stress-dependent barrier relationship [Eq. (5)] would lead to the linearly temperature-dependent CSS [Eq. (1)]. According to the transition state theory,<sup>45,46</sup> at a given applied shear stress  $\tau \rightarrow \tau_{c0}$ , the TB migration rate is

$$v_M = Nv_0 \exp\left(-\frac{E_{Cu}(\tau)}{k_B T}\right). \quad (7)$$



31 January 2024 14:02:53

**FIG. 8.** NEB results of TB migration in Cu. (a) Converged minimum energy path (MEP) of TB migration under the applied shear stress  $\tau = 2.5$  GPa. (b)–(d) Atomistic configurations along the MEP and their corresponding energies are plotted as red circles in (a). In (b)–(d), left figure shows the perspective view of simulation cell and right figure shows the top view of TB. Through the common neighbor analysis, a TB is displayed between the top and bottom surfaces by removing atoms with the perfect FCC structure. In (c) and (d), with TB migration in the negative Y direction, the disconnection nucleates in the form of elliptical shape (denoted by white atoms) and expands gradually to the entire TB area.

Here,  $v_0$  is the attempt frequency of twinning dislocation nucleation,  $N$  is the number of equivalent TB nucleation sites, and  $k_B$  is the Boltzmann constant. And  $E_{Cu}(\tau)$  is the TB migration barrier, which has been defined in Eq. (5). Then, the velocity of TB migration  $V_M$  has the form

$$V_M = H v_M = H N v_0 \exp\left(-\frac{E_{Cu}(\tau)}{k_B T}\right). \quad (8)$$

Since the TB is the shear-coupled GB, i.e.,

$$\beta = \frac{V}{V_M}. \quad (9)$$

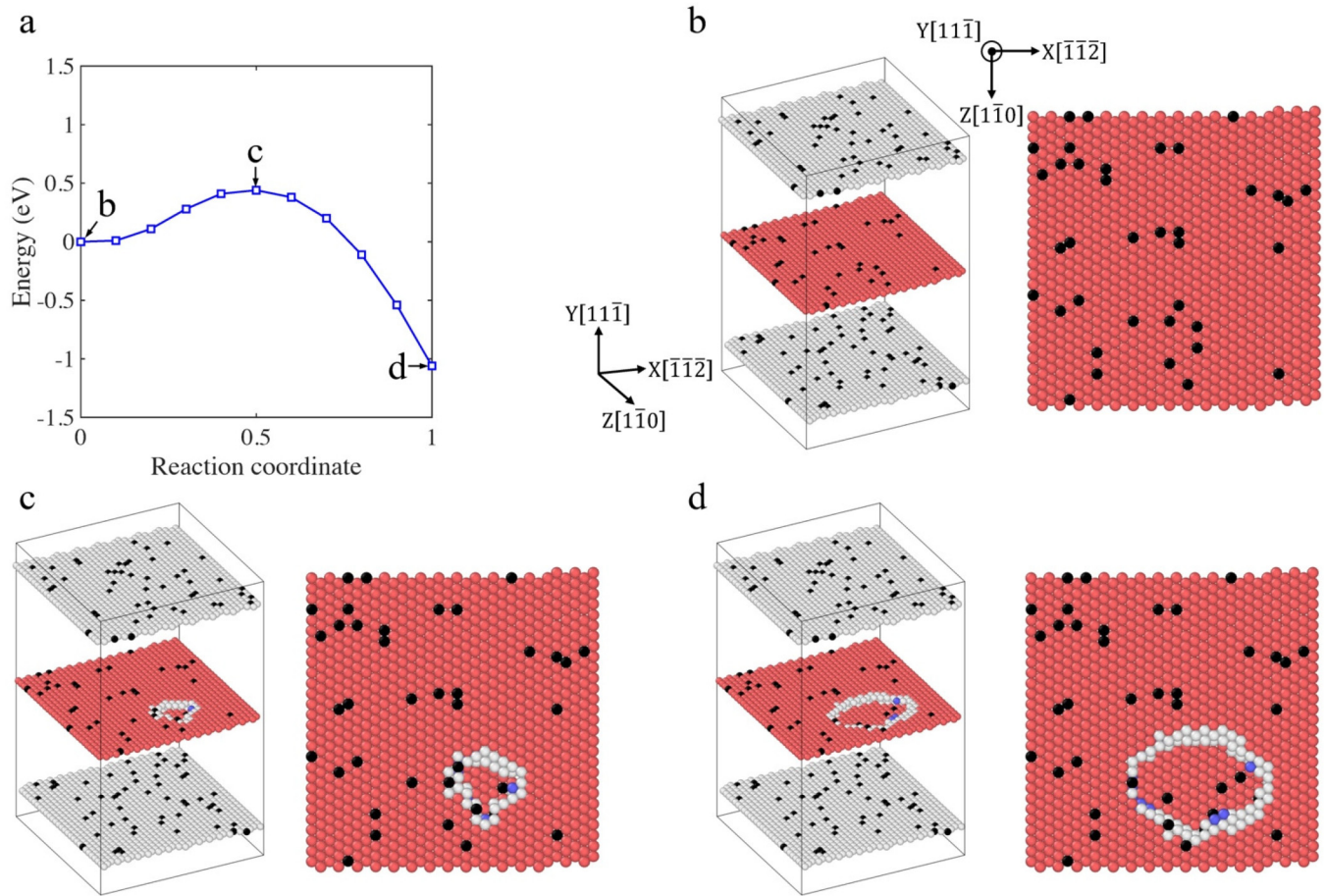
Here, the shear-coupled factor  $\beta$  has been defined in Sec. II, and the  $V$  is the constant velocity of the top slab rate with a value of  $0.01$  Å/ps.

Combining Eqs. (5), (8), and (9), we can obtain

$$\frac{\tau}{\tau_{c0}} = 1 - \frac{k_B T}{E_{Cu}^0} \ln\left(\frac{\beta H N v_0}{V}\right). \quad (10)$$

The Eq. (10) explains the linear relationship between CSS and temperature, as shown in Eq. (1). Comparing with Eqs. (1) and (9), we can obtain that the material constant  $A$  in Eq. (1) is given by  $A = \frac{k_B T_m}{E_{Cu}^0} \ln\left(\frac{\beta H N v_0}{V_s}\right)$ . Similarly, the linearly stress-dependent barrier





31 January 2024 14:02:53

**FIG. 9.** NEB results of TB migration in CuAg alloy with Ag fraction  $\chi = 0.05$ . (a) Converged MEP of TB migration under the applied shear stress  $\tau = 2.5$  GPa. (b)–(d) Atomistic configurations along the MEP and their corresponding energies are plotted as red circles in (a). Here, the Ag atoms are denoted by black dots.

relationship in CuAg [Eq. (6)] would lead to the linearly temperature-dependent CSS [Eq. (2)] through the similar derivation process.

#### IV. DISCUSSION

The underlying mechanism of Ag-induced reduction in the energy barrier of TB migration can be attributed to the Ag-enhanced homogeneous nucleation of partial dislocation. This effect may arise from a size misfit between Ag atoms (lattice parameter of 4.09 Å) and the matrix Cu atoms (lattice parameter of 3.615 Å). Ag chemical bonds facilitating dislocation nucleation may be another alternative explanation. In the context of the Cu–Ag system, both mechanical and chemical effects may contribute to the enhanced homogeneous dislocation nucleation. A systematic investigation of solute effects on homogeneous dislocation nucleation in Cu-based binary alloys

requires reliable DFT calculations, which are beyond the scope of this study.

This discovery challenges conventional wisdom, as solute atoms are traditionally regarded as GB migration inhibitors. However, the solute-enhanced TB migration mechanism may not be extended to other general GBs. NEB calculations demonstrate that the TB migration is controlled by the TB dislocation nucleation. The addition of solute atoms reduces the energy barrier of homogeneous dislocation nucleation, leading to enhanced TB migration. For general GBs, including some asymmetry or especially defective GBs, GB migration is accomplished through the nucleation and propagation of disconnections. There are numerous energy-favorable sites for disconnection nucleation. Consequently, it becomes evident that the controlling factor for GB migration may be the disconnection propagation as opposed to the disconnection nucleation. Hence, the presence of solute atoms would hinder the disconnection propagation and, consequently, impede GB migration.

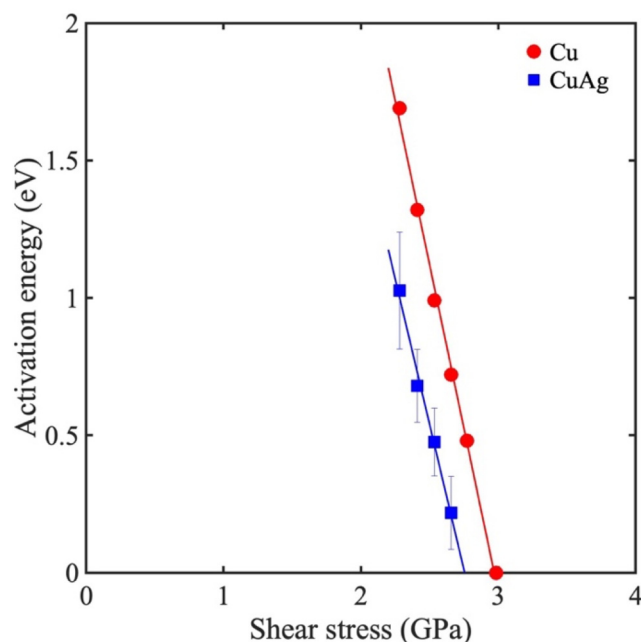


**FIG. 10.** Activation energies of TB migration vs shear stress in Cu and CuAg alloy with Ag fraction  $\chi = 0.05$ . The mean values for CuAg alloy are obtained by averaging the results from 10 samples with different randomly distributed Ag atoms. The error bars in the figure correspond to the standard deviation.

## V. CONCLUSIONS

In this study, we investigate the roles of temperature and solute on TB migration in pure Cu and CuAg alloys through atomistic simulations and theoretical analysis. Our MD simulations reveal that the critical shear stress of TB migration linearly decreases with increasing temperature for both Cu and CuAg alloys, which deviates from the classical exponential relationship reported in the literature. Surprisingly, our simulations also show that solute Ag atoms reduce the critical shear stress of TB migration in CuAg alloys, thereby facilitating TB migration. This observation challenges our intuition and conventional knowledge, as solute atoms are commonly considered to inhibit GB migration.

Through NEB calculations, we find that the activation energies of TB migration linearly decrease with shear stress as the applied shear stress approaches the critical shear stress, leading to the observed linear temperature dependencies through theoretical analysis. Moreover, the NEB results provide solid evidence that solute Ag atoms effectively lower the energy barrier of TB migration, providing an excellent explanation for the phenomenon of solute-enhanced TB migration.

This study opens new avenues for investigating the influence of various point defects on the migration and mobility of TB. Additionally, the NEB method utilized in this research can provide valuable insights into the impact of different types of alloy elements on GB migration and, consequently, the properties of polycrystalline materials in binary alloys or medium-/high-entropy alloys.

However, it is essential to consider that different GBs may exhibit varying deformation mechanisms. We plan to dedicate further efforts to explore these aspects in our future work.

## ACKNOWLEDGMENTS

The computations in this paper were run on the Siyuan-1 cluster supported by the Center for High Performance Computing at Shanghai Jiao Tong University. D. Chen acknowledges the support from the National Natural Science Foundation of China (No. 12272224).

## AUTHOR DECLARATIONS

### Conflict of Interest

The authors have no conflicts to disclose.

## Author Contributions

**Dengke Chen:** Conceptualization (equal); Formal analysis (equal); Funding acquisition (equal); Investigation (equal); Methodology (equal); Validation (equal); Visualization (equal); Writing – original draft (equal); Writing – review & editing (equal). **Yin Zhang:** Formal analysis (equal); Funding acquisition (equal); Investigation (equal); Methodology (equal); Validation (equal); Visualization (equal); Writing – original draft (equal); Writing – review & editing (equal). **Shuozhi Xu:** Conceptualization (equal); Methodology (equal); Validation (equal); Writing – review & editing (equal).

## DATA AVAILABILITY

The data that support the findings of this study are available from the corresponding author upon reasonable request.

## REFERENCES

- 1L. Lu, Y. Shen, X. Chen, L. Qian, and K. Lu, “Ultrahigh strength and high electrical conductivity in copper,” *Science* **304**(5668), 422–426 (2004).
- 2D. Jang, X. Li, and H. Gao, “Deformation mechanisms in nanotwinned metal nanopillars,” *Nat. Nanotechnol.* **7**, 594–601 (2012).
- 3Z. Cheng, H. Zhou, Q. Liu, H. Gao, and L. Lu, “Extra strengthening and work hardening in gradient nanotwinned metals,” *Science* **362**, eaau1925 (2018).
- 4S. Zhao, R. Zhang, Q. Yu, J. Ell, R. O. Ritchie, and A. M. Minor, “Cryoforged nanotwinned titanium with ultrahigh strength and ductility,” *Science* **373**, 1363–1368 (2021).
- 5A. A. Tiamiyu, E. L. Pang, X. Chen, J. M. LeBeau, K. A. Nelson, and C. A. Schuh, “Nanotwinning-assisted dynamic recrystallization at high strains and strain rates,” *Nat. Mater.* **21**, 786–794 (2022).
- 6Y. Zhu, X. Liao, and X. Wu, “Deformation twinning in nanocrystalline materials,” *Prog. Mater. Sci.* **1**(57), 1–62 (2012).
- 7P. Chowdhury and H. Sehitoglu, “Atomistic energetics and critical twinning stress prediction in face and body centered cubic metals: Recent progress,” *J. Eng. Mater. Technol.* **140**(2), 020801 (2018).
- 8Z. Wang, W. Lu, F. An, M. Song, D. Ponge, D. Raabe, and Z. Li, “High stress twinning in a compositionally complex steel of very high stacking fault energy,” *Nat. Commun.* **13**, 3598 (2022).
- 9K. Lu, L. Lu, and S. Suresh, “Strengthening materials by engineering coherent internal boundaries at the nanoscale,” *Science* **324**(5925), 349–352 (2009).

- <sup>10</sup>L. Lu, M. Dao, T. Zhu, and J. Li, "Size dependence of rate-controlling deformation mechanisms in nanotwinned copper," *Scr. Mater.* **60**(2), 1062–1066 (2009).
- <sup>11</sup>L. Zhu, H. Ruan, X. Li, M. Dao, H. Gao, and J. Lu, "Modeling grain size dependent optimal twin spacing for achieving ultimate high strength and related high ductility in nanotwinned metals," *Acta Mater.* **59**(14), 5544–5557 (2011).
- <sup>12</sup>T. Sinha and Y. Kulkarni, "Anomalous deformation in fcc metals at high temperatures," *J. Appl. Phys.* **109**, 114315 (2011).
- <sup>13</sup>J. Wang, A. Misra, and J. P. Hirth, "Shear response of  $\Sigma 3\{112\}$  twin boundaries in face-centered-cubic metals," *Phys. Rev. B* **83**, 064106 (2011).
- <sup>14</sup>K. D. Molodov and D. A. Molodov, "Grain boundary mediated plasticity: On the evaluation of grain boundary migration—Shear coupling," *Acta Mater.* **153**, 336–353 (2018).
- <sup>15</sup>J. W. Cahn, Y. Mishin, and A. Suzuki, "Coupling grain boundary motion to shear deformation," *Acta Mater.* **54**, 4953–4975 (2006).
- <sup>16</sup>M. I. Mendele and D. J. Srolovitz, "Impurity effects on grain boundary migration," *Model. Simul. Mater. Sci. Eng.* **10**, R79–R109 (2002).
- <sup>17</sup>H. Sun and C. Deng, "Direct quantification of solute effects on grain boundary motion by atomistic simulations," *Comput. Mater. Sci.* **93**, 137–143 (2014).
- <sup>18</sup>Y. Mishin, "Solute drag and dynamic phase transformations in moving grain boundaries," *Acta Mater.* **179**, 383–395 (2019).
- <sup>19</sup>R. K. Koju and Y. Mishin, "Direct atomistic modeling of solute drag by moving grain boundaries," *Acta Mater.* **198**, 111–120 (2020).
- <sup>20</sup>M. Alkayyali and F. Abdeljawad, "Grain boundary solute drag model in regular solution alloys," *Phys. Rev. Lett.* **127**, 175503 (2021).
- <sup>21</sup>A. Suhane, D. Scheiber, M. Popov, and V. I. Razumovskiy, "Solute drag assessment of grain boundary migration in Au," *Acta Mater.* **224**, 117473 (2022).
- <sup>22</sup>N. Du, Y. Qi, P. E. Krajewski, and A. F. Bower, "Aluminum  $\Sigma 3$  grain boundary sliding enhanced by vacancy diffusion," *Acta Mater.* **58**, 4245–4252 (2010).
- <sup>23</sup>D. Chen, S. Xu, and Y. Kulkarni, "Atomistic mechanism for vacancy-enhanced grain boundary migration," *Phys. Rev. Mater.* **4**, 033602 (2020).
- <sup>24</sup>D. Song, X. Li, J. Xue, H. Duan, and Z. Jin, "Irradiation-enhanced twin boundary migration in BCC Fe," *Philos. Mag. Lett.* **94**(6), 361–369 (2014).
- <sup>25</sup>J. Han, S. L. Thomas, and D. J. Srolovitz, "Grain-boundary kinetics: A unified approach," *Prog. Mater. Sci.* **98**, 386–476 (2018).
- <sup>26</sup>Q. Zhu, G. Cao, J. Wang, C. Deng, J. Li, Z. Zhang, and S. X. Mao, "In situ atomistic observation of disconnection-mediated grain boundary migration," *Nat. Commun.* **10**, 156 (2019).
- <sup>27</sup>C. Baruffi and W. A. Curtin, "Theory of spontaneous grain boundary roughening in high entropy alloys," *Acta Mater.* **234**, 118011 (2022).
- <sup>28</sup>Y. B. Wang, M. L. Sui, and E. Ma, "In situ observation of twin boundary migration in copper with nanoscale twins during tensile deformation," *Philos. Mag. Lett.* **87**(12), 935–942 (2007).
- <sup>29</sup>L. Zhang, W. Mao, M. Liu, and Y. Shibuta, "Mechanical response and plastic deformation of coherent twin boundary with perfect and defective structures," *Mech. Mater.* **141**, 103266 (2020).
- <sup>30</sup>Z. Zhang, M. M. Mao, J. Wang, B. Gludovatz, Z. Zhang, S. X. Mao, E. P. Georpe, Q. Yu, and R. O. Ritchie, "Nanoscale origins of the damage tolerance of the high-entropy alloy CrMnFeCoNi," *Nat. Commun.* **6**, 10143 (2015).
- <sup>31</sup>Z. Zhang, H. Sheng, Z. Wang, B. Gludovatz, Z. Zhang, E. P. Georpe, Q. Yu, S. X. Mao, and R. O. Ritchie, "Dislocation mechanisms and 3D twin architectures generate exceptional strength-ductility-toughness combination in CrCoNi medium-entropy alloy," *Nat. Commun.* **8**, 14390 (2017).
- <sup>32</sup>S. Huang, H. Huang, W. Li, D. Kim, S. Lu, X. Li, E. Holmstrom, S. K. Kwon, and L. Vitos, "Twinning in metastable high-entropy alloys," *Nat. Commun.* **9**, 2318 (2018).
- <sup>33</sup>E. P. George, W. A. Curtin, and C. C. Tasan, "High entropy alloys: A focused review of mechanical properties and deformation mechanisms," *Acta Mater.* **188**, 435–474 (2020).
- <sup>34</sup>A. Stukowski, "Visualization and analysis of atomistic simulation data with OVITO—The open visualization tool," *Model. Simul. Mater. Sci. Eng.* **18**(1), 015012 (2010).
- <sup>35</sup>A. P. Thompson, H. M. Aktulga, R. Berger, D. S. Bolintineanu, W. M. Brown, P. S. Crozier, P. J. in't Veld, A. Kohlmeyer, S. G. Moore, T. D. Nguyen, R. Shan, M. J. Stevens, J. Tranchida, C. Trott, and S. J. Plimpton, "LAMMPS—A flexible simulation tool for particle-based materials modeling at the atomic, meso, and continuum scales," *Comput. Phys. Commun.* **271**, 108171 (2022).
- <sup>36</sup>P. L. Williams, Y. Mishin, and J. C. Hamilton, "An embedded-atom potential for the Cu-Ag system," *Model. Simul. Mater. Sci. Eng.* **14**, 817–833 (2006).
- <sup>37</sup>R. K. Koju and Y. Mishin, "Relationship between grain boundary segregation and grain boundary diffusion in Cu-Ag alloys," *Phys. Rev. Mater.* **4**, 073403 (2020).
- <sup>38</sup>Q. An, W. L. Johnson, K. Samwer, S. L. Corona, and W. A. Goddard III, "Formation of two glass phases in binary Cu-Ag liquid," *Acta Mater.* **195**, 274–281 (2020).
- <sup>39</sup>N. Li, J. Wang, A. Misra, X. Zhang, J. Y. Huang, and J. P. Hirth, "Twinning dislocation multiplication at a coherent twin boundary," *Acta Mater.* **59**, 5989–5996 (2011).
- <sup>40</sup>J. A. Zimmerman, H. Gao, and F. F. Abraham, "Generalized stacking fault energies for embedded atom FCC metals," *Model. Simul. Mater. Sci. Eng.* **8**, 103–115 (2000).
- <sup>41</sup>Y. Su, S. Xu, and I. J. Beyerlein, "Density functional theory calculations of generalized stacking fault energy surfaces for eight face-centered cubic transition metals," *J. Appl. Phys.* **126**, 105112 (2019).
- <sup>42</sup>Q. Hu, L. Li, and N. M. Ghoniem, "Stick-slip dynamics of coherent twin boundaries in copper," *Acta Mater.* **57**, 4866–4873 (2009).
- <sup>43</sup>V. A. Ivanov and Y. Mishin, "Dynamics of grain boundary motion coupled to shear deformation: An analytical model and its verification by molecular dynamics," *Phys. Rev. B* **78**, 064106 (2008).
- <sup>44</sup>X. Li, H. Sun, Y. Pu, and C. Mi, "Extracting grain boundary motion in Cu-Al alloy from atomistic simulations," *J. Mater. Res.* **35**(20), 2701–2708 (2020).
- <sup>45</sup>T. Zhu, J. Li, A. Samanta, A. Leach, and K. Gall, "Temperature and strain-rate dependence of surface dislocation nucleation," *Phys. Rev. Lett.* **100**, 025502 (2008).
- <sup>46</sup>Q. Li, B. Xu, S. Hara, J. Li, and E. Ma, "Sample-size-dependent surface dislocation nucleation in nanoscale crystals," *Acta Mater.* **145**, 19–29 (2018).